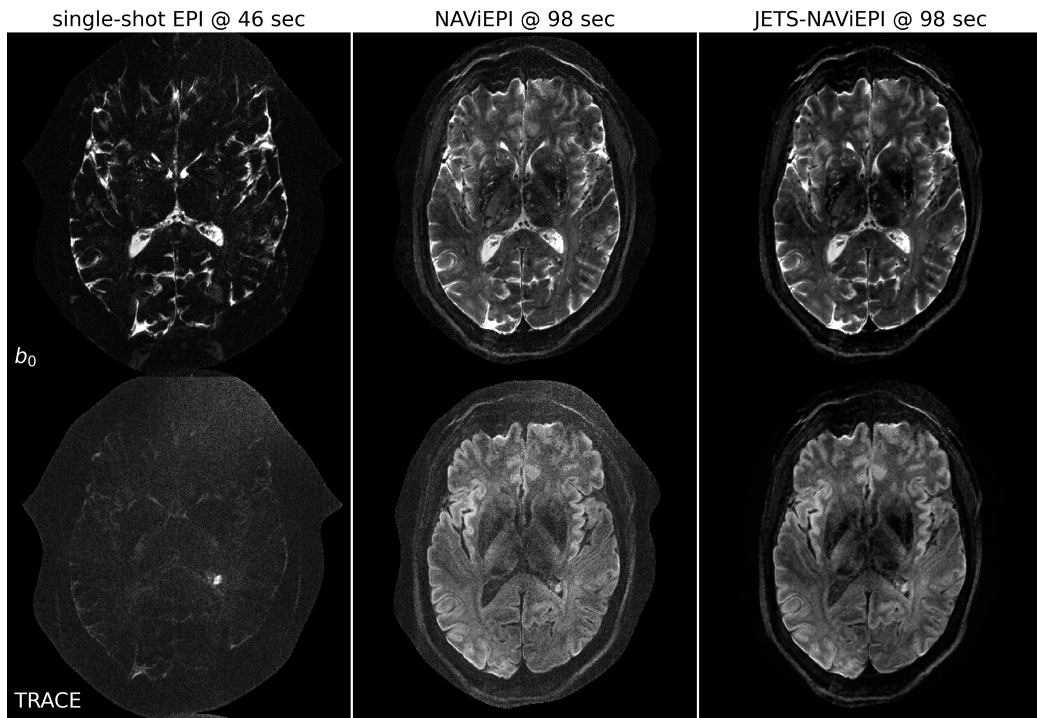


Graphical Abstract

Accelerated Diffusion Weighted Magnetic Resonance Imaging at 7 T: Joint Reconstruction for Shift-Encoded Navigator-based Interleaved Echo Planar Imaging (JETS-NAViEPI)

Zhengguo Tan, Patrick Alexander Liebig, Robin Martin Heidemann, Frederik Bernd Laun, Florian Knoll

3-scan trace acquisition with voxel size 0.5 X 0.5 X 2.0 mm³



Highlights

Accelerated Diffusion Weighted Magnetic Resonance Imaging at 7 T: Joint Reconstruction for Shift-Encoded Navigator-based Interleaved Echo Planar Imaging (JETS-NAViEPI)

Zhengguo Tan, Patrick Alexander Liebig, Robin Martin Heidemann, Frederik Bernd Laun, Florian Knoll

- Navigator-based interleaved EPI acquisition with minimal distortion mismatch between echoes
- Novel accelerated diffusion acquisition with shifted phase encoding among diffusion directions for complementary k - q -space sampling at 7 T
- Generalized joint k - q -slice diffusion-weighted image reconstruction with overlapping locally low-rank regularization
- Efficient simultaneous multi-slice (SMS) image reconstruction
- 3-scan trace acquisition with the voxel size $0.5 \times 0.5 \times 2.0 \text{ mm}^3$ and 60 slices at 1.5 min

Accelerated Diffusion Weighted Magnetic Resonance Imaging at 7 T: Joint Reconstruction for Shift-Encoded Navigator-based Interleaved Echo Planar Imaging (JETS-NAViEPI)

Zhengguo Tan^a, Patrick Alexander Liebig^b, Robin Martin Heidemann^b,
Frederik Bernd Laun^c, Florian Knoll^a

^a*Department Artificial Intelligence in Biomedical Engineering (AIBE),
Friedrich-Alexander University of Erlangen-Nuremberg, Erlangen, Germany*

^b*Siemens Healthcare GmbH, Erlangen, Germany*

^c*Institute of Radiology, University Hospital Erlangen, Friedrich-Alexander University of Erlangen-Nuremberg, Erlangen, Germany*

Abstract

The pursuit of high spatial-angular-temporal resolution for in vivo diffusion-weighted magnetic resonance imaging (DW-MRI) at ultra-high field strength (7 T and above) is important in understanding brain microstructure and function. Such pursuit, however, faces several technical challenges. First, increased off-resonance and shorter T_2 relaxation require faster echo train readouts. Second, existing high-resolution DW-MRI techniques usually employ in-plane fully-sampled multi-shot EPI, which not only prolongs the scan time but also induces a high specific absorption rate (SAR) at 7 T. To address these challenges, we develop in this work navigator-based interleaved EPI (NAViEPI) which enforces the same effective echo spacing (ESP) between the imaging and the navigator echo. First, NAViEPI renders no distortion mismatch between the two echoes, and thus simplifies shot-to-shot phase variation correction. Second, NAViEPI allows for a large number of shots

(e.g. > 4) with undersampled iEPI acquisition, thereby rendering clinically-feasible high-resolution sub-millimeter protocols. To retain signal-to-noise ratio (SNR) and to reduce undersampling artifacts, we developed a k_y -shift encoding among diffusion encodings to explore complementary k - q -space sampling. Moreover, we developed a novel joint reconstruction with overlapping locally low-rank regularization generalized to the multi-band multi-shot acquisition at 7 T (dubbed JETS-NAViEPI). Our method was demonstrated with experimental results covering 1 mm isotropic resolution multi b -value DWI and sub-millimeter in-plane resolution fast TRACE acquisition.

Keywords: Diffusion-weighted magnetic resonance imaging, Echo planar imaging, Navigator, Ultra-high field, Joint reconstruction, Low rank, Simultaneous multi slice

¹ **1. Introduction**

² Diffusion-weighted magnetic resonance imaging (DW-MRI) ([Le Bihan et al., 1986; Merboldt et al., 1985](#)) is a non-invasive modality that is sensi-
³ tive to the intravoxel Brownian motion of water molecules. DW-MRI forms
⁴ the basis for diffusion tensor imaging (DTI) ([Basser et al., 1994; Mori et al., 1999](#)) and high angular resolution diffusion imaging (HARDI) ([Tuch et al., 2002](#)), and has been widely used in acute brain ischemia diagnosis, in tumor
⁵ detection and staging, and in neuroscience ([Jones, 2010](#)).

⁶ For DW-MRI acquisition, the commonly used pulse sequence is single-
⁷ shot echo-planar imaging (SS-EPI) ([Mansfield, 1977](#)). SS-EPI is capable of
⁸ rapidly acquiring one DW image per radio-frequency excitation at the order
⁹ of 100 ms, and is thus motion robust. However, conventional SS-EPI, even
¹⁰ with three-fold accelerated acquisition ([Bammer et al., 2001](#)) using parallel
¹¹ imaging ([Roemer et al., 1990; Ra and Rim, 1993; Pruessmann et al., 1999](#);
¹² [Griswold et al., 2002](#)), still suffers from low spatial resolution and geometric
¹³ distortions.

¹⁴ In the quest for high spatial-angular-temporal-resolution and minimal-
¹⁵ geometry-distortion DW-MRI, tremendous efforts have been made. Tech-
¹⁶ niques [for](#) the correction of image distortions induced by off-resonances and R249.Minor.5
¹⁷ eddy currents have been developed ([Andersson et al., 2003](#)). Furthermore,
¹⁸ gSlider ([Setsompop et al., 2018](#)) with blipped-CAIPI ([Setsompop et al., 2012](#))
¹⁹ for simultaneous multi-slice (SMS) ([Maudsley, 1980; Breuer et al., 2005](#))
²⁰ was proposed to achieve high-resolution DW-MRI. Advanced pulse sequences
²¹ based on multi-shot EPI have also been developed, including but not limited
²² to interleaved EPI (iEPI) ([Butts et al., 1993](#)), PROPELLER ([Pipe et al., 2004](#)),

26 2002), and readout-segmented EPI (rsEPI) (Porter and Heidemann, 2009;
27 Heidemann et al., 2010).

28 Based on four-shot iEPI, multiplexed sensitivity encoding (MUSE) image
29 reconstruction achieved DW-MRI with a sub-millimeter in-plane resolution
30 and maximal b -value 800 s/mm^2 at 3 T (Chen et al., 2013). The four-shot
31 iEPI employed in MUSE acquired an in-plane fully-sampled k -space, except
32 partial Fourier. Every shot (segment), corresponding to four-fold under-
33 sampling, was then reconstructed via parallel imaging to obtain shot-to-shot
34 phase variation. This indicates that increasing the number of shots in MUSE
35 will result in higher undersampling per shot, and consequently, degrade shot
36 phase estimation (Wu and Miller, 2017). On the other hand, the use of in-
37 plane fully-sampled four-shot iEPI is challenging at ultra-high field (e.g. 7 T),
38 because the SAR is linearly proportional to the square of the field strength.

39 Alternatively, navigator-based iEPI acquisition has been proposed (Jeong
40 et al., 2013; Dai et al., 2017, 2018). These proposals allow for a larger num-
41 ber of shots, and hence higher spatial resolution. However, due to the use of
42 different ESP between the imaging echo and the navigator echo, these propos-
43 als suffered from geometric distortion mismatch between the two echoes and
44 thus required specific compensation methods. In contrast, rsEPI (Porter and
45 Heidemann, 2009; Heidemann et al., 2010) used the same readout segment
46 for both echoes, and thus required no correction of the navigator echo.

47 Beyond the MUSE-type parallel imaging reconstruction, compressed sens-
48 ing (Lustig et al., 2007; Block et al., 2007) has been explored. For instance,
49 multi-shot reconstruction techniques based on structured low-rank matrix
50 completion (MUSSELS) (Mani et al., 2017; Bilgic et al., 2019) achieved 5-

shot DW-MRI with 9-fold undersampling per shot. Recently, JULEP (Dai et al., 2023) incorporated explicit phase mapping into MUSSELS. These reconstruction techniques, i.e., MUSE, MUSSELS and JULEP, targeted the reconstruction of one DW image from interleaved EPI acquisition, and did not explore joint- k - q -space undersampling or reconstruction.

Joint- k - q -space undersampling can be achieved via proper regularization along the diffusion encoding direction. Relevant examples are diffusion undersampling with Gaussian process estimated reconstruction (DAGER) (Wu et al., 2019) and magnitude-based spatial-angular locally low-rank regularization (SPA-LLR) (Hu et al., 2020). However, DAGER addressed the reconstruction problem of single-shot EPI acquisition and SPA-LLR focused on the reconstruction of single-band and fully-sampled iEPI acquisition.

R248.Major.2

In this work, we propose a Joint k - q -slice rEconsTruction framework for Shift-encoded NAVigator-based interleaved EPI at 7 T (dubbed JETS-NAVIEPI). Our pulse sequence, NAVIEPI, differs from most existing techniques. First, NAVIEPI builds upon interleaved EPI, thereby allowing for fast and efficient k -space coverage. Second, inspired by rsEPI, NAVIEPI ensures the same effective ESP between the imaging and the navigator echo, thereby minimizing geometric distortion and allowing for the use of a larger number of shots. NAVIEPI essentially integrates the advantages of both iEPI and rsEPI. Third, NAVIEPI utilizes undersampled multi-shot iEPI, thereby alleviating the SAR problem at 7 T. Fourth, NAVIEPI shifts the k -space in-plane sampling pattern along the phase encoding (k_y) direction. This shifting creates complementary k - q -space sampling, which leads to the possibility of our joint k - q -slice reconstruction. Specifically, we employ spatial-diffusion

⁷⁶ overlapping LLR regularization to jointly reconstruct all diffusion encodings
⁷⁷ and multi-band slices. In vivo experiments at 7 T and comparisons with other
⁷⁸ techniques demonstrate the efficiency of our proposed method in achieving
⁷⁹ high spatial resolution DW-MRI at ultra-high field.

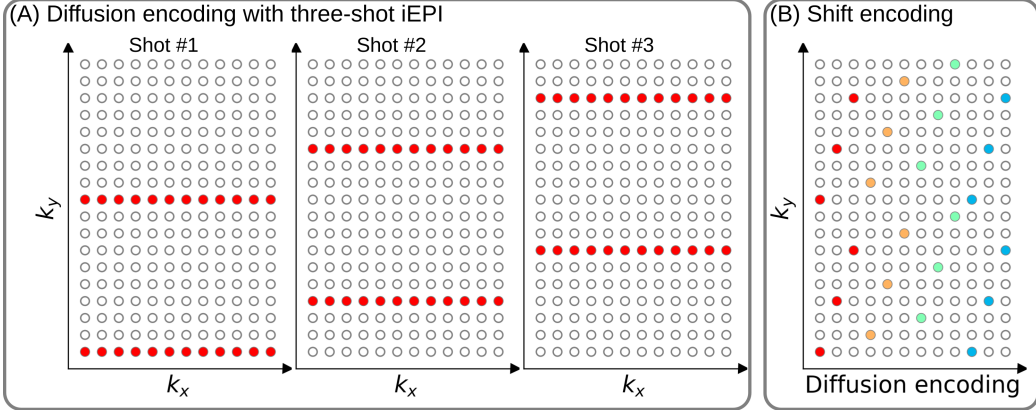


Figure 1: (A) An example DW-MRI acquisition with three-shot interleaved EPI acquisition. (B) The proposed k_y shifted diffusion encoding scheme. This example employs three shots per DW image. Therefore, every three columns have the same color.

80 2. Materials and methods

81 2.1. Multi-band shift-encoded iEPI acquisition

82 Fig. 1 (A) displays the diffusion-weighted image acquisition based on
 83 three-shot interleaved EPI with three-fold in-plane undersampling. Conven-
 84 tionally, such a sampling pattern is repeated for all diffusion directions. In
 85 contrast, we propose the k_y -shifted diffusion encoding, as shown in Fig. 1 (B).
 86 The interleaved EPI sampling pattern is shifted by one k_y line per diffusion
 87 direction, with the cycling period being the in-plane undersampling factor.

88 It is worth noting that, as shown in Fig. 1 (A), the undersampling factor
 89 of one segment is $R_{\text{in-plane}} \times N_{\text{shot}}$ (ignore multi-band undersampling here),
 90 yielding nine-fold in-plane undersampling in this example. In other words,
 91 the undersampling factor per segment linearly scales up with the number
 92 of shots. Consequently, conventional self-gating reconstruction techniques,
 93 e.g. MUSE, suffer from degraded shot-to-shot phase estimation, which in

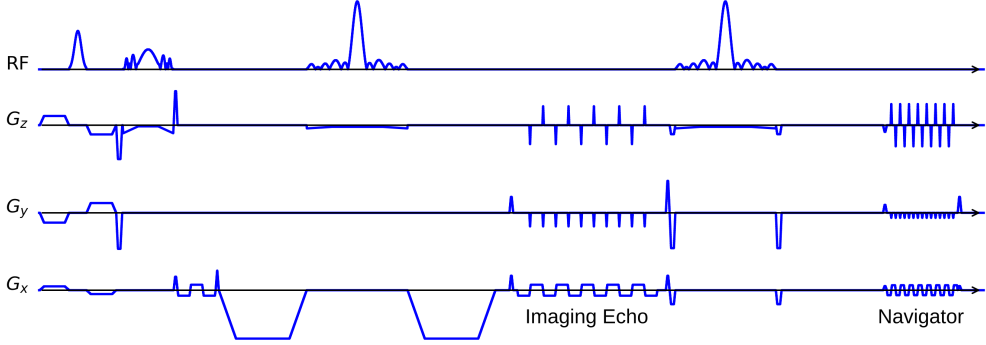


Figure 2: The NAViEPI sequence diagram. SMS is utilized for the acquisition of both imaging and navigator echoes. While the acceleration factor per navigator is the same as listed in Table 1, the acceleration factor per imaging echo is in addition linearly scaled by the number of shots.

94 turn limits the number of shots and spatial resolution.

95 *2.2. NAViEPI: Navigator-based iEPI with consistent effective ESP between
96 the imaging and the navigator echo - where iEPI meets rsEPI*

97 Instead of the self-gated MUSE with in-plane fully-sampled iEPI and
98 a limited number of shots, We propose NAVigator-based interleaved EPI
99 (NAViEPI), as illustrated in Fig. 2. Moreover, inspired by rsEPI (Porter and
100 Heidemann, 2009), NAViEPI enforces a consistent effective ESP between the
101 imaging and the navigator echo, thereby minimizing distortion mismatch
102 between the two echoes.

103 Since one imaging echo presents one segment in multi-shot EPI acquisi-
104 tion, its effective ESP is defined as

$$\text{ESP}_{\text{eff}} = \frac{\text{ESP}}{R_{\text{in-plane}} \times N_{\text{shot}}} \quad (1)$$

105 Here, a larger number of shots (segments) increases the undersampling factor
106 per segment (see Fig. 1), but decreases the effective ESP. Since the navigator

107 echo is acquired for each segment, its in-plane undersampling factor equals
108 $R_{\text{in-plane}}$. Therefore, the effective ESP of the navigator echo must match that
109 of the imaging echo, as given in Eq. (1). With a matching effective ESP, the
110 base resolution of the navigator echo can then be determined.

111 *2.3. In vivo acquisition protocols*

112 We implemented multiple in-vivo acquisition protocols at a clinical 7 T
113 MR system (MAGNETOM Terra, Siemens Healthineers, Erlangen, Ger-
114 many) equipped with a 32-channel head coil (Nova Medical, Wilmington,
115 MA, USA) and the XR-gradient system (maximum gradient strength 80 mT/m
116 with a peak slew rate of 200 T/m/s). To calibrate coil sensitivity maps, refer-
117 ence scans employed a gradient-echo (GRE) sequence. Spectral fat saturation
118 and mono-polar diffusion-encoding gradients were used. The phase-encoding
119 direction was selected as anterior-to-posterior.

Table 1: NAViEPI acquisition protocols

Protocol	1.0 mm isotropic		sub-millimeter	
	#1	#2	#3	#4
Diffusion mode	MDDW ¹		3-scan trace	
Diffusion scheme	monopolar			
Diffusion direction	20	114	3	
<i>b</i> -value (s/mm ²)	1000	3-shell ²	1000	
<i>b</i> ₀	0	12	1	
FOV (mm ²)	200		220	
In-plane resolution (mm ²)	1.0		0.5	
Slice thickness (mm)	1.0		2.0	
Slices	141	114	60	
Navigator	No	No	Yes	No
Shots	4	2	5	1
TR (ms)	7700	5200	4400	8000
TEs (ms)	67	66	58/95.1	143
ESP (ms)	1.02	0.81	1.52	1.48
Bandwidth (Hz/Pixel)	1086	1460	758	
Partial Fourier			6/8	
Acceleration ³	1 × 3	3 × 3	3 × 2	
TA (min) ⁴	10 : 42	22 : 25	1 : 38	0 : 46

¹ MDDW: Multi-direction diffusion weighting;² 3-shell: 20, 30, and 64 directions with *b*-values of 1000, 2000, and 3000 s/mm², respectively;³ Acceleration: Both in-plane and slice undersampling can be employed, denoted as (*R*_{in-plane} × *R*_{slice});⁴ TA: Total acquisition time.

121 This study was approved by the local ethics committee. Three volunteers
122 with informed consent obtained before scanning participated in this study.
123 Detailed acquisition protocols are listed in Table 1.

124 *2.3.1. 20-diffusion-direction acquisition at 1 mm isotropic resolution*

125 As listed in Table 1, Protocol #1 with four-shot iEPI and without in- R248.Major.1a
126 plane undersampling was implemented. This protocol represents the acquisi-
127 tion scheme employed in many existing multi-shot reconstruction techniques,
128 (e.g., MUSE, SPA-LLR, and JULEP). The acquired data from this protocol
129 served as ground truth. Different reconstruction methods, specifically JETS,
130 MUSE, and JULEP were compared. We compared with JULEP instead of R249.Minor.6
131 MUSSELS, because JULEP uses not only structured low-rank constraints R248.Major.3a
132 but also explicit phase mapping.

133 We then retrospectively reduced the four-shot data to only one shot per R248.Major.1b
134 diffusion encoding without and with the proposed k_y shifting to simulate
135 four-fold in-plane undersampling. JETS reconstruction was performed on R248.Major.1b
136 the fully-sampled data and the retrospectively undersampled data to validate
137 the proposed k_y -shifted acquisition. R248.Major.1c

138 *2.3.2. Three-shell direction acquisition at 1 mm isotropic resolution*

139 Protocol #2 in Table 1 was implemented for multi-shell diffusion tensor R248.Major.3c
140 imaging (DTI) (Basser et al., 1994). We acquired a total of 114 diffusion
141 directions, whereas b_0 measurements were interspersed every ten diffusion
142 directions. This protocol was used to demonstrate the capability of of JETS
143 in achieving high spatial-angular-temporal resolution.

144 2.3.3. 3-scan trace acquisition at $0.5 \times 0.5 \times 2.0 \text{ mm}^3$ voxel size

145 As listed in Table 1, Protocol #3 was implemented based on NAViEPI
146 with five shots per diffusion encoding. This protocol was compared against
147 single-shot EPI (Protocol #4) with the same spatial resolution and acceler-
148 ation, such as to demonstrate the sampling efficiency of NAViEPI.

149 2.4. Forward modeling

150 Our proposed acquisition method yields multi-dimensional multi-band
151 k -space data $\mathbf{y}_{c,q,s}$, where c, q, s denotes the index of the coil sensitivity
152 map, the diffusion encoding, and the shot, respectively. Acquisition modeling
153 needs to consider several aspects.

154 First, the acquired k -space data \mathbf{y} is mapped from individual shot images
155 $\mathbf{x}_{q,s,z}$ via the forward model,

$$\begin{aligned}\mathbf{y}_{c,q,s} &= \mathbf{P}_{q,s} \boldsymbol{\Sigma} \boldsymbol{\Theta}_z \mathbf{F} \mathbf{S}_c \mathbf{x}_{q,s,z} \\ \mathbf{y} &:= \mathbf{E}_1 \mathbf{x}\end{aligned}\tag{2}$$

156 Here, the encoding matrix \mathbf{E}_1 comprises a chain of linear operators. Every
157 shot image \mathbf{x} is point-wise multiplied by a set of coil sensitivity maps (\mathbf{S}) and
158 Fourier transformed (\mathbf{F}). The output is then point-wise multiplied by the
159 multi-slice phase map ($\boldsymbol{\Theta}$) with z the slice index in simultaneously excited
160 slices. This operator shifts individual slice along the phase-encoding direction
161 via varying phase modulation (Breuer et al., 2005). The SMS k -space data
162 is then summed (collapsed, $\boldsymbol{\Sigma}$) along the slice dimension and masked (point-
163 wise multiplied, \mathbf{P}) by the sampling pattern of each diffusion encoding and
164 shot.

165 Second, for diffusion MRI based on multi-shot EPI, multiple shots ac-
 166 quired for a given diffusion encoding need to be combined as one DW image
 167 ($\tilde{\mathbf{x}}$). One possibility is to perform magnitude average (Chen et al., 2013)
 168 or root-sum-squares (RSS) (Mani et al., 2017) of shot images. This method R249.Minor.7
 169 is robust to in-plane motion, but sub-optimal concerning SNR (Guhaniyogi
 170 et al., 2016). Alternatively, shot combination can be done via shot-to-shot
 171 phase variation correction (Liu et al., 2005; Chen et al., 2013). This can be
 172 incorporated into our formulation as point-wise multiplication between the R249.Minor.8
 173 shot-to-shot phase variation (Φ) and the DW image ($\tilde{\mathbf{x}}$),

$$\mathbf{x}_{q,s,z} = \Phi_{q,s,z} \tilde{\mathbf{x}}_{q,z} \quad (3)$$

174 Note that $\tilde{\mathbf{x}}$ can be obtained by applying the adjoint of Φ to \mathbf{x} . In MUSE,
 175 Φ is obtained by parallel imaging reconstruction of all shots with subsequent
 176 phase smoothing of every shot image. Based on this phase correction, the
 177 complete forward model follows

$$\mathbf{y} := \mathbf{E}_2 \tilde{\mathbf{x}} = \mathbf{E}_1 \Phi \tilde{\mathbf{x}} \quad (4)$$

178 where the encoding matrix \mathbf{E}_2 comprises the chain of the shot-to-shot phase
 179 variation Φ and the encoding matrix \mathbf{E}_1 . We implemented these two encoding
 180 matrices in SigPy (Ong and Lustig, 2019).

181 *2.5. Joint k - q -slice reconstruction*

182 Based on the generalized forward models in Eqs. (2) and (4), our proposed
 183 joint k - q -slice reconstruction can be formulated as a three-step approach.

184 **I. Navigator echo reconstruction.** The acquisition of navigator echoes
 185 follows the forward model in Eq. (2), so the reconstruction of navigator

186 echoes can be formulated as:

$$\operatorname{argmin}_{\mathbf{x}} \|\mathbf{y} - \mathbf{E}_1 \mathbf{x}\|_2^2 + \lambda \mathbf{R}(\mathbf{x}) \quad (5)$$

187 where $\mathbf{R}(\mathbf{x})$ denotes the regularization functional with the regularization
188 strength λ . In this work, ℓ^2 regularization was used, i.e., $\mathbf{R}(\mathbf{x}) =$
189 $\|\mathbf{x}\|_2^2$. In the case of self-navigating (i.e., no navigator acquired) as Pro-
190 tocol #2, the central k -space region (i.e., 1/4 of the full image matrix)
191 of each segment is used as \mathbf{y} in Eq. (5).

192 **II. Iterative phase smoothing.** Shot-to-shot phase variation was ex-
193 tracted from the reconstructed navigator echo phases. Assuming that
194 phase images are spatially smooth (Chen et al., 2013; Dai et al., 2023),
195 we employed the iterative approach to smooth phase,

$$\mathbf{x}^{(k+1)} = \mathbf{F}^{-1} \mathcal{H} \mathbf{F} \mathbf{x}^{(k)} \quad (6)$$

196 where the index k denotes the phase smoothing iteration step, and $x^{(0)}$
197 is then the reconstructed navigator image from Step I. \mathcal{H} is the Hanning R248.Minor.12
198 window.

199 **III. Shot-combined reconstruction.** Joint reconstruction of all DW im-
200 ages using the shot-combined forward model \mathbf{E}_2 with shot-to-shot phase
201 variation from Step II reads:

$$\operatorname{argmin}_{\tilde{\mathbf{x}}} \|\mathbf{y} - \mathbf{E}_2 \tilde{\mathbf{x}}\|_2^2 + \lambda \|\mathbf{T}(\tilde{\mathbf{x}})\|_* \quad (7)$$

202 Here, LLR regularization was employed in the local spatial-diffusion ma-
203 trices, based on the theory of partially separable functions (Liang, 2007;
204 Trzasko and Manduca, 2011; Zhang et al., 2015). \mathbf{T} represents a linear

operator that firstly slides a local patch window through all DW images
and then flattens every set of local patches to construct two-dimensional
(2D) spatial-diffusion matrices. The spatial dimension equals the block
size, and the diffusion dimension is the number of diffusion encodings.
 $\|\mathbf{T}(\tilde{\mathbf{x}})\|_*$ is the nuclear norm, i.e. the sum of singular values of a spatial-
diffusion matrix. This nuclear norm regularization was accomplished
via singular value thresholding (SVT) of each spatial-diffusion matrix R248.Minor.6
(Cai et al., 2010). After SVT, the adjoint of \mathbf{T} , \mathbf{T}^H , was needed to
reorder pixel values from the spatial-diffusion matrices back to DW im-
ages. To alleviate checkerboard artifacts induced by LLR regularization
with non-overlapping blocks (Hu et al., 2020), we employed overlapping
blocks. In this case, values from overlapping positions are summed up
to the output of \mathbf{T}^H . To enable the correct use of \mathbf{T}^H , we element-wise
divided the output of \mathbf{T}^H by a scaling matrix. This matrix was obtained
via $\mathbf{T}^H(\mathbf{T}(\mathbf{1}))$, where $\mathbf{1}$ denotes the matrix of all ones with the same
shape as the input \mathbf{x} . R249.Minor.9

221 2.6. Reconstruction

222 The acquired raw data was read in by twixtools (<https://github.com/pehses/twixtools>). Ramp-sampling regridding and FOV/2-ghost correc-
223 tion were also performed in twixtools. Subsequently, coil sensitivity maps
224 were computed from reference scans using ESPIRiT (Uecker et al., 2014) in
225 SigPy (Ong and Lustig, 2019).

227 With this pre-processing as well as the implemented forward models and
228 proximal operator, the inverse problem in Eq. (7) was solved by the alter-
229 nating direction method of multipliers (ADMM) (Boyd et al., 2010).

230 ADMM solves the minimization problems in an alternating update scheme,

$$\begin{cases} \mathbf{x}^{(k+1)} := \underset{\mathbf{x}}{\operatorname{argmin}} \| \mathbf{y} - \mathbf{E}(\mathbf{x}) \|^2 + \rho/2 \| \mathbf{T}\mathbf{x} - \mathbf{z}^{(k)} + \mathbf{u}^{(k)} \|_2^2 \\ \mathbf{z}^{(k+1)} := \mathcal{T}_{\lambda/\rho}(\mathbf{T}\mathbf{x}^{(k+1)} + \mathbf{u}^{(k)}) \\ \mathbf{u}^{(k+1)} := \mathbf{u}^{(k)} + \mathbf{T}\mathbf{x}^{(k+1)} - \mathbf{z}^{(k+1)} \end{cases} \quad (8)$$

231 where k denotes the ADMM iteration. \mathbf{z} is the auxiliary variable ($\mathbf{z} = \mathbf{T}\mathbf{x}$),
232 and \mathbf{u} is the Lagrangian multipliers. Importantly, when solving Eq. (2), \mathbf{x}
233 denotes shot images and \mathbf{E} denotes \mathbf{E}_1 in Eq. (8). In contrast, \mathbf{x} denotes shot-
234 combined images and \mathbf{E} denotes \mathbf{E}_2 when solving Eq. (4). \mathbf{x} can be solved
235 using linear least square algorithms, e.g. conjugate gradients (Hestenes and
236 Stiefel, 1952), while \mathbf{z} is updated via singular value thresholding (\mathcal{T}) with
237 the thresholding parameter λ/ρ . The coupling parameter ρ is effective in
238 both the update of \mathbf{x} and \mathbf{z} . It acts as Tikhonov regularization strength
239 when updating \mathbf{x} , but also inversely scales the thresholding strength when
240 updating \mathbf{z} , as shown in Supporting Information Figures S1 and S2.

241 In this work, 15 ADMM iterations with $\rho = 0.05$ and $\lambda = 0.04$, and a
242 block size of 6 for LLR (refer to Supporting Information Figure S3) were
243 used. All reconstructions were done on a single A100 SXM4/NVLink GPU
244 with 40 GB memory (NVIDIA, Santa Clara, CA, USA).

245 We compared our proposed joint reconstruction with established multi-
246 shot reconstruction techniques, specifically, MUSE (Chen et al., 2013) and
247 JULEP (Dai et al., 2023), hosted on GitHub by Dr. Dai (Dai et al., 2023).
248 Further, we performed the local-PCA denoising (Cordero-Grande et al., 2019)
249 as implemented in MRtrix (Tournier et al., 2019) on the MUSE reconstructed
250 complex DW images.

251 With reconstructed DW images from Protocol #2 in Table 1, color-coded

²⁵² fractional anisotropy (cFA) maps ([Basser et al., 1994](#)) were fitted using DiPy
²⁵³ ([Garyfallidis et al., 2014](#)),

254 **3. Results**

255 *3.1. Iterative smoothing of shot-to-shot phase variation*

256 Navigators were acquired with the acceleration rate as listed in Table 1.
257 Besides, the base resolution of navigators (e.g. 32 in Protocol #3 in Table 1)
258 was smaller than imaging echoes. As a result, reconstructed navigator phases
259 (refer to the first column in Fig. 3) from Step I in Section 2.5 are not spatially
260 smooth. Such phases, when used in the shot-combined reconstruction, result
261 in signal void artifacts in DW images. To address this problem, we utilized
262 the iterative smoothing procedure. As shown in Fig. 3, the ripple-like phase
263 artifact disappears after five iterations. It can also be seen that such an R249.Minor.11
264 iterative procedure retains the shot-to-shot phase variation.

– 12

265 *3.2. Comparison to MUSE and JULEP with four-shot iEPI acquisition*

266 The iterative phase smoothing was also applicable to MUSE-type self-
267 navigating reconstruction, where shot phases were reconstructed from imag-
268 ing echoes. Fig. 4 compares our proposed JETS with MUSE (Chen et al.,
269 2013), MUSE with complex-valued local-PCA denoiser (Cordero-Grande et al.,
270 2019), and JULEP (Dai et al., 2023). The residual noise from MUSE can be
271 largely removed by the denoiser. However, when compared to JETS, the de-
272 noiser shows residual noise patterns within the globus pallidus (indicated by
273 the red arrow). JETS also shows better denoising than JULEP. The reason
274 is that JETS enforces spatial-diffusion regularization, whereas JULEP for-
275 mulates structured low-rank regularization of the four shots for one diffusion
276 encoding.

Iterative smoothing of shot-to-shot phase variation

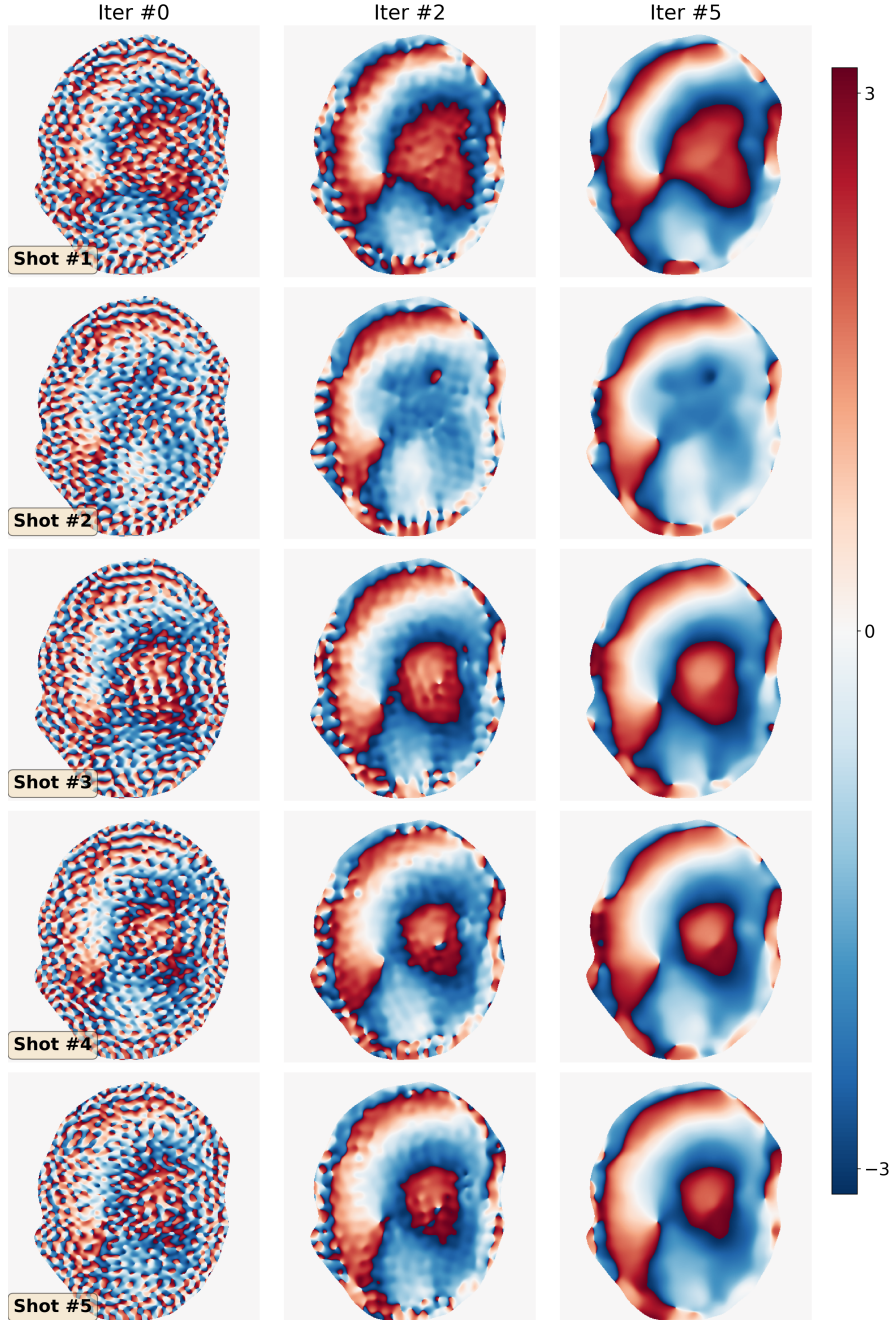


Figure 3: Iterative smoothing of shot-to-shot phase variation according to Eq. (6). Navigators from Protocol #3 were reconstructed based on Step I in Section 2.5 and then used as the input (iter #0, left column).

8th DW image from 4-shot iEPI @ 1 mm ISO

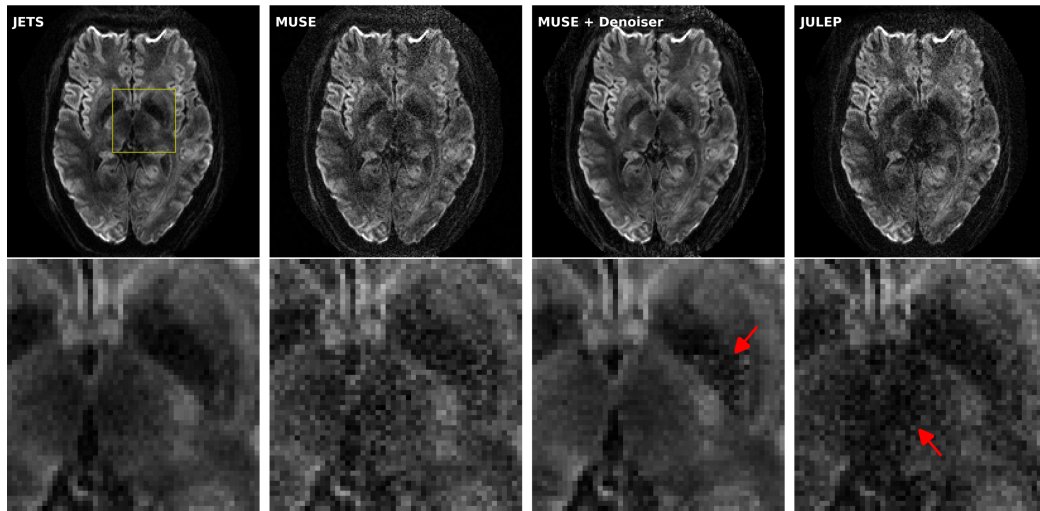


Figure 4: Reconstructed DW images (the 8th diffusion encoding) based on 4-shot iEPI acquisition with 1 mm isotropic resolution (Protocol #1 in Table 1). Four reconstruction methods are compared (from left to right): JETS, MUSE, MUSE with denoiser, and JULEP. The 2nd row displays the magnified views of the yellow square. The image from the denoiser (3rd column) shows residual noise patterns within the globus pallidus (indicated by the red arrow). The JULEP reconstruction (4th column) shows signal dropout in the central region (indicated by the red arrow).

R249.Minor.13

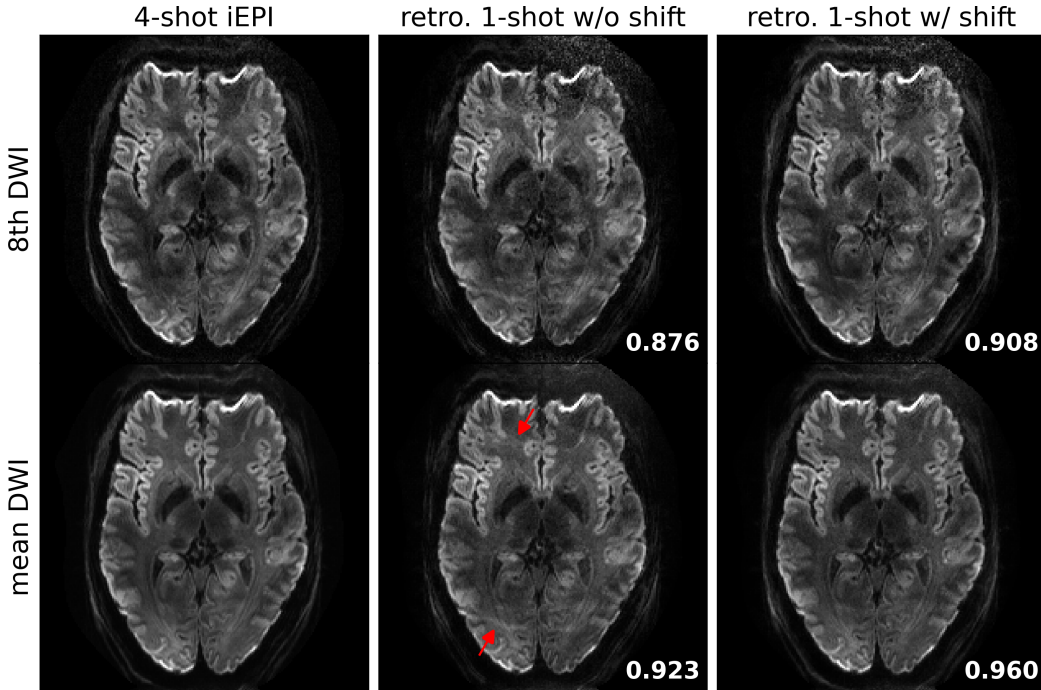


Figure 5: Quantitative validation of the proposed k_y -shift encoding sampling pattern based on 4-shot iEPI acquisition with 1 mm isotropic resolution (Protocol #1 in Table 1). (Top) the 8th diffusion encoding and (bottom) mean DWI over 20 diffusion encodings. (1st column) JETS reconstruction of 4-shot iEPI acquisition is used as the ground truth. The 2nd and the 3rd column displays JETS reconstruction of retrospectively undersampled 1-shot acquisition without and with k_y shifting, respectively. Residual aliasing artifacts are visible in the reconstruction without k_y shifting, as indicated by the red arrows. Structural similarity (SSIM) values are computed and displayed in the bottom right corners.

R249.Minor.14

- 16

277 3.3. Retrospectively undersampling from the four-shot iEPI acquisition

278 JETS reconstruction results on the four-shot prospectively fully-sampled
279 data from Protocol #1 in Table 1, as well as on the retrospectively under-
280 sampled one-shot data without and with the proposed k_y shift are displayed
281 in Fig. 5. Residual aliasing artifacts are visible in the reconstruction without
282 k_y shifting, as indicated by the red arrows. In contrast, the reconstruction R249.Minor.17
283 with the proposed k_y shifting among diffusion encodings shows much reduced R249.Minor.18
284 aliasing, reduced noise, and higher SSIM.

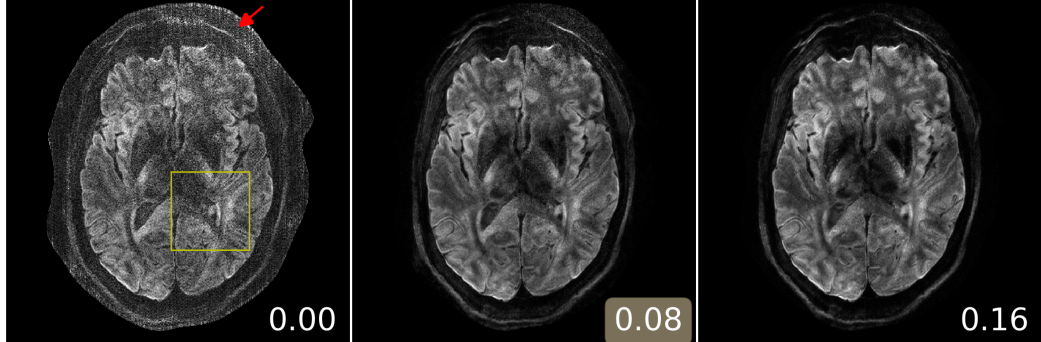
285 3.4. Analysis of reconstruction parameters

286 Here we provide a systematic analysis of the proposed JETS reconstruc-
287 tion with LLR regularization applied to the spatial-diffusion dimension, as
288 shown in Fig. 6.

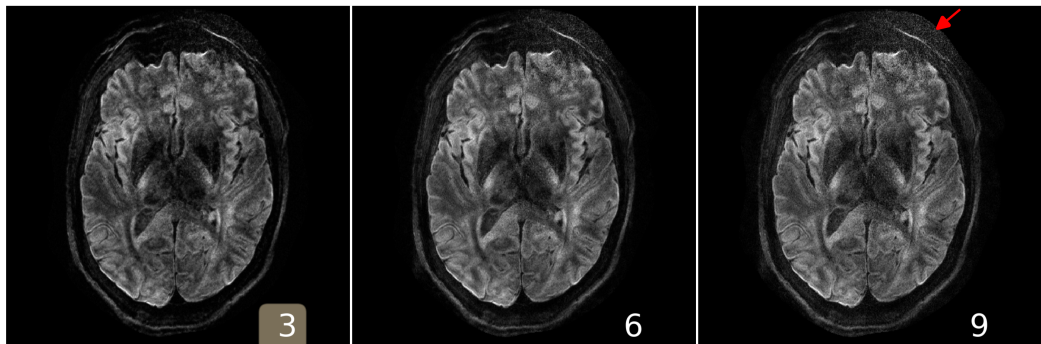
289 First, we varied the regularization strength λ . We tested values of 0, 0.08,
290 and 0.16. The reconstruction with $\lambda = 0$ in Eq. (7) corresponds to parallel R249.Minor.19
291 imaging reconstruction without LLR regularization. It is worth noting that
292 the proposed NAViEPI sequence demonstrates high-quality sub-millimeter
293 DW images ($0.5 \times 0.5 \times 2.0 \text{ mm}^3$ in this example). The DW images can be
294 further improved with the use of LLR regularization, i.e., reduced noise, as
295 seen in the reconstruction with $\lambda = 0.08$. Increasing λ (e.g. 0.16) further
296 reduces noise, but at the cost of increased blurring. Therefore, $\lambda = 0.08$ was
297 selected in this work.

298 Second, besides the regularization strength, the block size (i.e., the area
299 of 2D patches) also plays a role in denoising. We employed square blocks in
300 this work. Here, the block width of 2 shows the best denoising as compared
301 to 1 and 3, especially in the peripheral brain region. Among the three tested

(A) varying λ , keeping block as 6 and stride as 1



(B) varying block size, keeping λ as 0.08 and stride as 1



(C) varying stride, keeping λ as 0.08 and block as 6

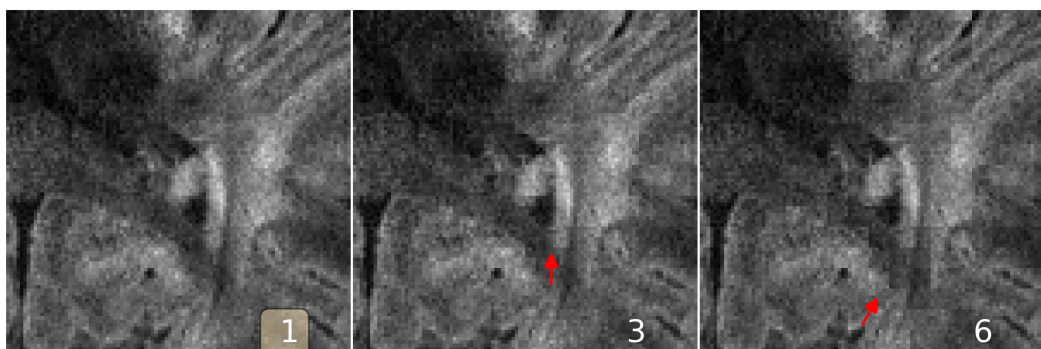


Figure 6: Analysis of reconstruction parameters based on the 3-scan trace acquisition with $0.5 \times 0.5 \times 2.0 \text{ mm}^3$ (Protocol #3 in Table 1). Displayed are JETS reconstructed single-direction DW images. **(A)** Varying the regularization strength λ from 0 to 0.08 and 0.16. **(B)** Varying the block size from 3 to 6 and 9. **(C)** Varying the stride size from 1 to 3 and 6 (non-overlapping).

302 block widths, the block size of 4 (with the block width 2) is the smallest one
303 which is no smaller than the diffusion directions in this 3-scan trace example
304 (1 b_0 plus 3 orthogonal diffusion directions). This observation agrees with
305 the suggestion that the patch size should be no smaller than and close to the
306 diffusion directions (Cordero-Grande et al., 2019).

307 Third, we varied the stride, i.e., the step from one local patch to the
308 next. The use of overlapping LLR (Fig. 6 (C) left) better suppresses blocky
309 artifacts, compared to the partially overlapping LLR (Fig. 6 (C) middle) and
310 the non-overlapping LLR (Fig. 6 (C) right).

R248.Major.4b

311 3.5. Sampling efficiency of NAViEPI

312 As shown in Fig. 7, NAViEPI achieves sub-millimeter resolution (voxel
313 size $0.5 \times 0.5 \times 2.0 \text{ mm}^3$) with the use of a 5-shot acquisition. When compared
314 to a single-shot acquisition with the same voxel size, the acquisition time of
315 NAViEPI is about two times longer, but the image quality of NAViEPI is
316 remarkably improved.

R249.Minor.22

317 In the sub-millimeter imaging scenario, the increased base resolution re-
318 quires longer TE (143 ms) in the single-shot acquisition, which results in
319 significant signal loss due to T_2 relaxation. Therefore, sub-millimeter DWI
320 necessitates multi-shot acquisition, which is subject to shot-to-shot phase
321 variation and long scan time. However, NAViEPI solves both challenges. The
322 5-shot acquisition reduces TE to 58 ms, and thus retains SNR significantly
323 compared to the single-shot acquisition. Moreover, the JETS reconstruction
324 can help to reduce noise and improve structural visibility.

325 Fig. 8 shows the JETS reconstructed b_0 and TRACE images in different
326 slice locations. Admittedly, the lower brain region (e.g. slice #22) exhibits in-

3-scan trace acquisition with voxel size $0.5 \times 0.5 \times 2.0 \text{ mm}^3$

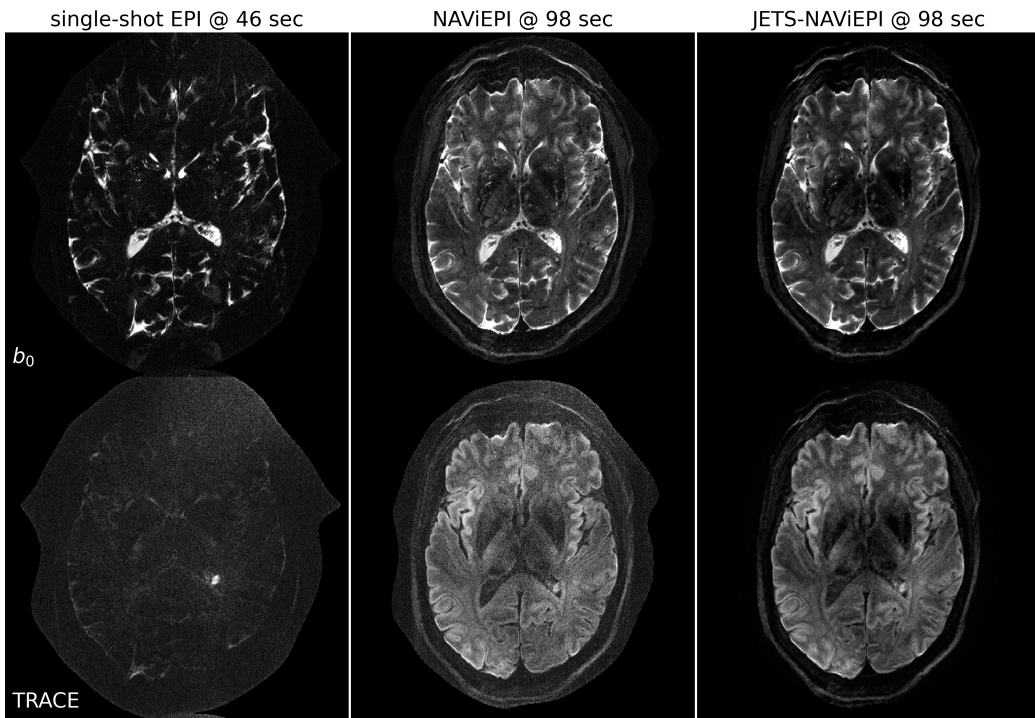


Figure 7: Sampling efficiency of the proposed NAViEPI sequence. 5-shot NAViEPI acquisition with the voxel size $0.5 \times 0.5 \times 2.0 \text{ mm}^3$ (Protocol #3) was compared with single-shot EPI acquisition (Protocol #4). Both the 1st and the 2nd columns were reconstructed via parallel imaging without LLR regularization, whereas the 3rd column was reconstructed via JETS.

3-scan trace acquisition with voxel size $0.5 \times 0.5 \times 2.0 \text{ mm}^3$

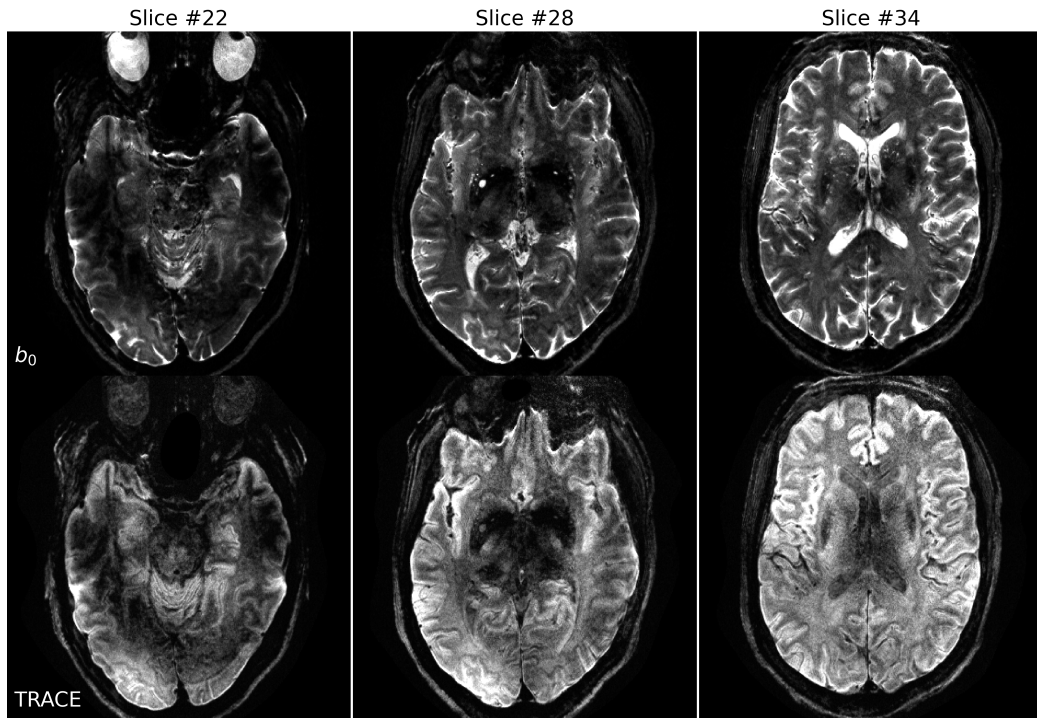


Figure 8: Reconstruction of the 3-scan trace acquisition with the voxel size $0.5 \times 0.5 \times 2.0 \text{ mm}^3$ (Protocol #3) at different slices.

327 homogeneous and lower signal intensity than the upper slices. Such inhomogeneity can be alleviated with the use of multi-channel parallel transmission
328 (Katscher et al., 2003; Grissom et al., 2010).

330 *3.6. Diffusion tensor imaging*

331 Since 30 diffusion encodings were acquired in Protocol #2, the block size
332 in LLR regularization was lifted to 6, such that the spatial-diffusion matrix
333 for SVT has similar width and height. The other parameter were kept the
334 same as found in Fig. 6.

335 The mean DWIs in Fig. 9 illustrate high spatial resolution and high SNR.
336 In line with Fig. 8, we can notice the signal loss in the cerebellum region, due
337 to the use of single-channel transmission in this work. On the other hand,
338 the reconstructed cFA maps in Fig. 9 show clear fiber orientation in all ori-
339 entations. Moreover, tiny fiber structures can be visualized in the zoomed-in
340 cFA maps. Because of the low signal sensitivity surrounding the cerebellum,
341 residual artifacts are visible in the zoomed-in sagittal view. To enhance the
342 DTI fitting performance, one possibility is to acquire more diffusion encod-
343 ings.

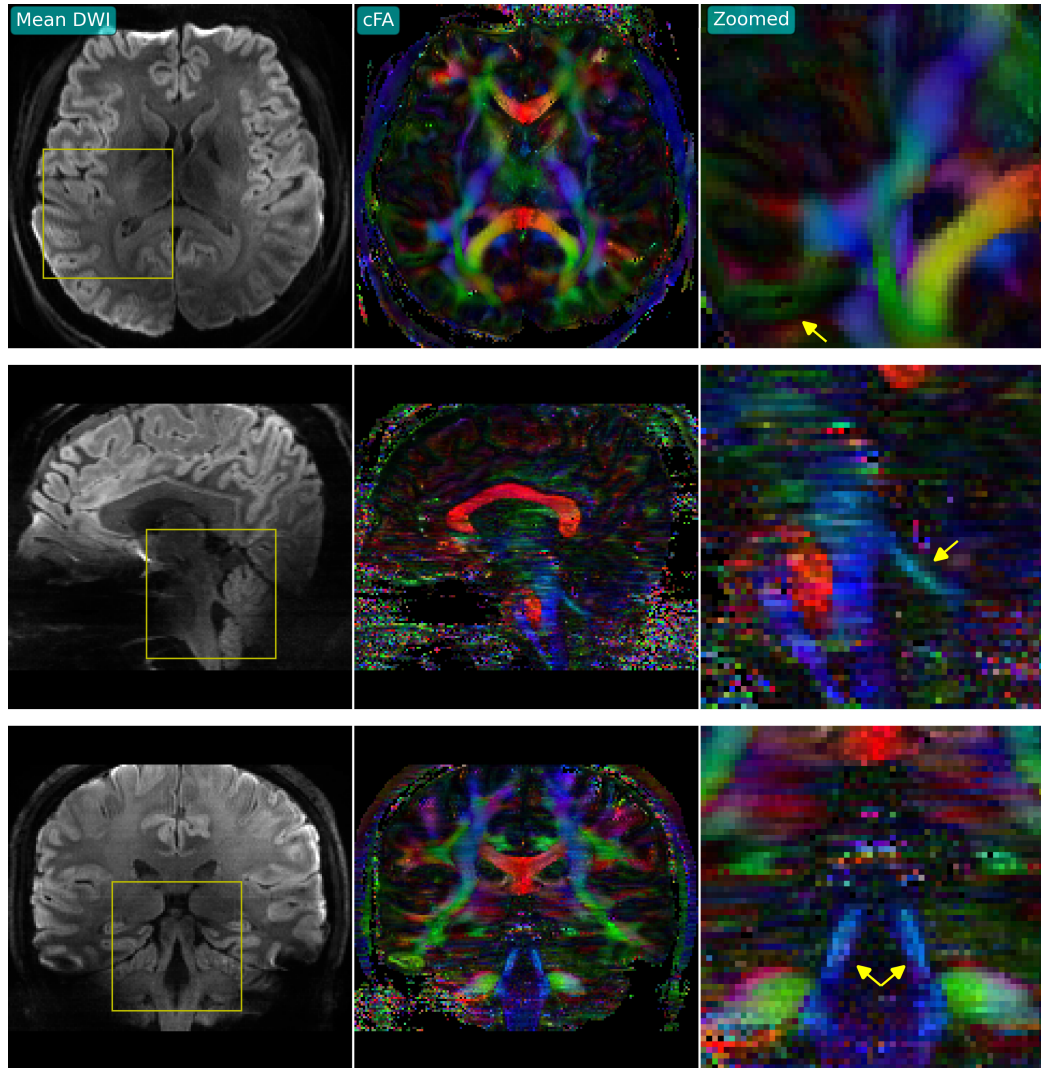


Figure 9: (Left) Mean DWI, (middle) cFA, and (right) cFA in the zoomed-in region based on JETS reconstructed DWI from Protocol #2. Three orthogonal slices (transversal, sagittal, and coronal) are displayed from top to bottom.

344 **4. Discussion**

345 This work reports a novel DW-MRI technique, JETS-NAViEPI. NAViEPI
346 (1) achieves the fast and efficient acquisition of both imaging and navigator
347 echoes, (2) enforces consistent effective ESP between the two echoes, and (3)
348 allows for undersampled iEPI as well as a large number of shots. Moreover,
349 compared to the single-shot acquisition, joint k - q -slice reconstruction with k_y -
350 shift encoding on NAViEPI retains SNR and reduces aliasing artifacts in DW
351 images. As a result, JETS-NAViEPI renders high spatiotemporal resolution
352 diffusion MRI protocols in 7 T, e.g., a 3-scan trace acquisition with the voxel
353 size $0.5 \times 0.5 \times 2.0 \text{ mm}^3$ at 1.5 min.

R249.Minor.24

354 One limitation of JETS-NAViEPI is the long reconstruction time due to
355 the simultaneous reconstruction of all DW images and the use of overlapping
356 locally low-rank regularization. The reconstruction for the Protocol #3 in
357 Table 1 on an A100 GPU takes about 2 min per multi-band slice. To reduce
358 the computation time, coil compression algorithms (Buehrer et al., 2007;
359 Huang et al., 2008) can be employed to reduce the number of coils for image
360 reconstruction. Moreover, one can deploy multi-GPU distributed computing
361 or modern optimization algorithms (e.g. stochastic gradient descent) (Ong
362 et al., 2020) to speed up the reconstruction.

363 Neither the signal modeling in Eqs. (2) and (4) nor the LLR regularization
364 considers the subject motion. In the presence of motion, the regularized
365 reconstruction can degrade. To overcome this problem, scout-informed motion
366 estimation and reconstruction (Polak et al., 2022) could be integrated
367 into the framework.

368 Another potential extension of this work is to incorporate distortion cor-

369 rection. The standard distortion correction method is known as TOPUP
370 (Andersson et al., 2003), which acquires two scans with opposing phase-
371 encoding directions to obtain the field inhomogeneity map and then performs
372 conjugate phase reconstruction to correct for distortion. Alternatively, the
373 multi-echo acquisition could be used for the coil sensitivity reference scan,
374 such that both coil sensitivity and B_0 field inhomogeneity maps could be
375 reconstructed from the data.

R249.Minor.25

376 This work employed a single regularization weight λ to enforce low rank-
377 ness along the spatial-diffusion direction. However, SNR may be heteroge-
378 neous within the FOV. Therefore, one single regularization scalar may be
379 inadequate to cover the whole FOV. Beyond this SVT-based reconstruction,
380 one can seek to use machine learning to learn a q -space prior as the regularizer
381 (Hammernik et al., 2018; Lam et al., 2019; Mani et al., 2021).

R249.Minor.26

382 Although NAViEPI employs navigators for the acquisition of shot-to-
383 shot phase variation, it is worth noting that phase behavior depends on
384 several hard-to-control factors such as pulsatile motion, bulk motion, loca-
385 tions within the brain, and diffusion sensitization strength. Therefore, more
386 comprehensive modeling or post-processing such as image registration can
387 be considered in future work.

388 potential synergies between their LLR and the denoiser

R248.3b

389 While this work reconstructs all DW images and then performs model
390 fitting, an alternative approach is to directly estimate b_0 and diffusion ten-
391 sors from measured k - q -space data using model-based reconstruction (Knoll
392 et al., 2015; Dong et al., 2018; Shafieizargar et al., 2023). Compared to DW
393 image reconstruction, model-based reconstruction solves for a fewer number

394 of unknowns, but requires strict diffusion tensor modeling and the use of
395 nonlinear least square solvers.

396 **5. Conclusions**

397 We demonstrated the JETS-NAViEPI technique, which integrates a k_y -
398 shifted encoding interleaved EPI sequence and a joint reconstruction with
399 overlapping locally low-rank regularization for high spatial-angular-temporal
400 resolution DW-MRI at 7 T. This technique allows for high-quality DW image
401 reconstruction with accelerated acquisitions.

402 **Funding**

403 This work was supported by Deutsche Forschungsgemeinschaft (DFG) –
404 Project Number 513220538, as well as National Institutes of Health (NIH)
405 R01 EB024532 and P41 EB017183.

406 **Data and code available statement**

407 In the spirit of reproducible and open science, we publish our source
408 code (<https://github.com/ZhengguoTan/sigpy>) as well as the raw k -space
409 data (<https://doi.org/10.5281/zenodo.7548595>). We also provide inter- R248.8
410 active demonstrations of the reconstruction procedure (https://github.com/ZhengguoTan/demo_jets_diffusion_mri_7t).
411

412 **Acknowledgments**

413 The authors gratefully acknowledge the scientific support and HPC re-
414 sources provided by the Erlangen National High Performance Computing

415 Center (NHR@FAU) of Friedrich-Alexander-Universität Erlangen-Nürnberg
416 (FAU) under the NHR project b143dc. NHR funding is provided by federal
417 and Bavarian state authorities. NHR@FAU hardware is partially funded by
418 the German Research Foundation (DFG) – 440719683.

419 The authors thank Dr. Peter Neher for the discussion on MITK-Diffusion.
420 The authors thank Dr. Berkin Bilgic for making the MUSSELS source code
421 (<https://bit.ly/2QgBg9U>) publically available, Dr. Erpeng Dai for sharing
422 the JULEP source code (<https://github.com/daiep/JULEP>) on GitHub,
423 and Dr. Zhiyong Zhang for sharing the SPA-LLR source code (<https://github.com/ZZgroupSJTU/PMcmsDTI>) on GitHub. The authors also thank
424 Dr. Philipp Ehses for the discussion on the use of twixtools (<https://github.com/pehses/twixtools>).
425

427 References

- 428 Andersson, J.L.R., Skare, S., Ashburner, J., 2003. How to correct suscepti-
429 bility distortions in spin-echo echo-planar images: application to diffusion
430 tensor imaging. NeuroImage 20, 870–888. doi:[10.1016/S1053-8119\(03\)00336-7](https://doi.org/10.1016/S1053-8119(03)00336-7).
- 432 Bammer, R., Keeling, S.L., Augustin, M., Pruessmann, K.P., Wolf, R., Stoll-
433 berger, R., Hartung, H.P., Fazekas, F., 2001. Improved diffusion-weighted
434 single-shot echo-planar imaging (EPI) in stroke using sensitivity encoding
435 (SENSE). Magn. Reson. Med. 46, 548–554. doi:[10.1002/mrm.1226](https://doi.org/10.1002/mrm.1226).
- 436 Basser, P.J., Mattiello, J., Le Bihan, D., 1994. MR diffusion tensor

- 437 spectroscopy and imaging. Biophys. J. 66, 259–267. doi:[10.1016/S0006-3495\(94\)80775-1](https://doi.org/10.1016/S0006-3495(94)80775-1).
- 438
- 439 Bilgic, B., Chatnuntawech, I., Manhard, M.K., Tian, Q., Liao, C., Iyer, S.S.,
440 Cauley, S.F., Huang, S.Y., Polimeni, J.R., Wald, L.L., Setsompop, K.,
441 2019. Highly accelerated multishot echo planar imaging through synergistic
442 machine learning and joint reconstruction. Magn. Reson. Med. 82, 1343–
443 1358. doi:[10.1002/mrm.27813](https://doi.org/10.1002/mrm.27813).
- 444 Block, K.T., Uecker, M., Frahm, J., 2007. Undersampled radial MRI with
445 multiple coils. Iterative image reconstruction using a total variation con-
446 straint. Magn. Reson. Med. 57, 1186–1098. doi:[10.1002/mrm.21236](https://doi.org/10.1002/mrm.21236).
- 447 Boyd, S., Parikh, N., Chu, E., Peleato, B., Eckstein, J., 2010. Distributed
448 optimization and statistical learning via the alternating direction method
449 of multipliers. Foundations and Trends in Machine Learning 3, 1–122.
450 doi:[10.1561/2200000016](https://doi.org/10.1561/2200000016).
- 451 Breuer, F.A., Blaimer, M., Heidemann, R.M., Mueller, M.F., Griswold, M.A.,
452 Jakob, P.M., 2005. Controlled aliasing in parallel imaging results in higher
453 acceleration (CAIPIRINHA) for multi-slice imaging. Magn. Reson. Med.
454 53, 684–691. doi:[10.1002/mrm.20401](https://doi.org/10.1002/mrm.20401).
- 455 Buehrer, M., Pruessmann, K.P., Boesiger, P., Kozerke, S., 2007. Array com-
456 pression for MRI with large coil arrays. Magn. Reson. Med 57, 1131–1139.
457 doi:[10.1002/mrm.21237](https://doi.org/10.1002/mrm.21237).
- 458 Butts, K., Riederer, S.J., Ehman, R.L., Thompson, R.M., Jack, C.R., 1993.

- 459 Interleaved echo planar imaging on a standard MRI system. *Magn. Reson.*
460 *Med.* 31, 67–72. doi:[10.1002/mrm.1910310111](https://doi.org/10.1002/mrm.1910310111).
- 461 Cai, J.F., Candès, E.J., Shen, Z., 2010. A singular value thresholding
462 algorithm for matrix completion. *SIAM. J. Optim.* 20, 1956–1982.
463 doi:[10.1137/080738970](https://doi.org/10.1137/080738970).
- 464 Chen, N.K., Guidon, A., Chang, H.C., Song, A.W., 2013. A robust multi-
465 shot scan strategy for high-resolution diffusion weighted MRI enabled by
466 multiplexed sensitivity-encoding (MUSE). *NeuroImage* 72, 41–47. doi:[10.1016/j.neuroimage.2013.01.038](https://doi.org/10.1016/j.neuroimage.2013.01.038).
- 468 Cordero-Grande, L., Christiaens, D., Hutter, J., Price, A.N., Hajnal, J.V.,
469 2019. Complex diffusion-weighted image estimation via matrix recovery
470 under general noise models. *NeuroImage* 200, 391–404. doi:[10.1016/j.neuroimage.2019.06.039](https://doi.org/10.1016/j.neuroimage.2019.06.039).
- 472 Dai, E., Ma, X., Zhang, Z., Yuan, C., Guo, H., 2017. Simultaneous multislice
473 accelerated interleaved EPI DWI using generalized blipped-CAIPI acqui-
474 sition and 3D K-space reconstruction. *Magn. Reson. Med.* 77, 1593–1605.
475 doi:[10.1002/mrm.26249](https://doi.org/10.1002/mrm.26249).
- 476 Dai, E., Mani, M., McNab, J.A., 2023. Multi-band multi-shot diffu-
477 sion MRI reconstruction with joint usage of structured low-rank con-
478 straints and explicit phase mapping. *Magn. Reson. Med.* 89, 95–111.
479 doi:[10.1002/mrm.29422](https://doi.org/10.1002/mrm.29422).
- 480 Dai, E., Zhang, Z., Ma, X., Dong, Z., Li, X., Xiong, Y., Yuan, C., Guo, H.,
481 2018. The effects of navigator distortion and noise level on interleaved EPI

- 482 DWI reconstruction: a comparison between image- and k -space method.
483 Magn. Reson. Med. 80, 2024–2032. doi:[10.1002/mrm.27190](https://doi.org/10.1002/mrm.27190).
- 484 Dong, Z., Dai, E., Wang, F., Zhang, Z., Ma, X., Yuan, C., Guo, H., 2018.
485 Model-based reconstruction for simultaneous multislice and parallel imag-
486 ing accelerated multishot diffusion tensor imaging. Med. Phys. 45, 3196–
487 3204. doi:[10.1002/mp.12974](https://doi.org/10.1002/mp.12974).
- 488 Garyfallidis, E., Brett, M., Amirmekian, B., Rokem, A., van der Walt, S.,
489 Descoteaux, M., Nimmo-Smith, I., Contributors, D., 2014. DIPY, a library
490 for the analysis of diffusion MRI data. Front. Neuroinform. 8, 1–17. doi:[10.3389/fninf.2014.00008](https://doi.org/10.3389/fninf.2014.00008).
- 491
- 492 Grissom, W.A., Sacolick, L., Vogel, M.W., 2010. Improving high-field MRI
493 using parallel excitation. Imaging Med. 2, 675–693. doi:[10.2217/IIM.10.62](https://doi.org/10.2217/IIM.10.62).
- 494
- 495 Griswold, M.A., Jakob, P.M., Heidemann, R.M., Nittka, M., Jellus, V.,
496 Wang, J., Kiefer, B., Haase, A., 2002. Generalized autocalibrating par-
497 tially parallel acquisitions (GRAPPA). Magn. Reson. Med. 47, 1202–1210.
498 doi:[10.1002/mrm.10171](https://doi.org/10.1002/mrm.10171).
- 499
- 500 Guhaniyogi, S., Chu, M.L., Chang, H.C., Song, A.W., Chen, N.K., 2016. Mo-
501 tion immune diffusion imaging using augmented MUSE for high-resolution
502 multi-shot EPI. Magn. Reson. Med. 75, 639–652. doi:[10.1002/mrm.25624](https://doi.org/10.1002/mrm.25624).
- 503 Hammernik, K., Klatzer, T., Kobler, E., Recht, M.P., Sodickson, D.K., Pock,
504 T., Knoll, F., 2018. Learning a variational network for reconstruction of

- 504 accelerated MRI data. Magn. Reson. Med. 79, 3055–3071. doi:[10.1002/mrm.26977](https://doi.org/10.1002/mrm.26977).
- 505
- 506 Heidemann, R.M., Porter, D.A., Anwander, A., Feiweier, T., Heberlein, K.,
507 Knösche, T.R., Turner, R., 2010. Diffusion imaging in humans at 7 T
508 using readout-segmented EPI and GRAPPA. Magn. Reson. Med. 64, 9–
509 14. doi:[10.1002/mrm.22480](https://doi.org/10.1002/mrm.22480).
- 510 Hestenes, M.R., Stiefel, E., 1952. Methods of conjugate gradients for solving
511 linear systems. J. Res. Natl. Bur. Stand. 49, 409–436. doi:[10.6028/jres.049.044](https://doi.org/10.6028/jres.049.044).
- 512
- 513 Hu, Y., Wang, X., Tian, Q., Yang, G., Daniel, B., McNab, J., Hargreaves, B.,
514 2020. Multi-shot diffusion-weighted MRI reconstruction with magnitude-
515 based spatial-angular locally low-rank regularization (SPA-LLR). Magn.
516 Reson. Med. 83, 1596–1607. doi:[10.1002/mrm.28025](https://doi.org/10.1002/mrm.28025).
- 517 Huang, F., Vijayakumar, S., Li, Y., Hertel, S., Duensing, G.R., 2008. A soft-
518 ware channel compression technique for faster reconstruction with many
519 channels. Magn. Reson. Imaging 26, 133–141. doi:[10.1016/j.mri.2007.04.010](https://doi.org/10.1016/j.mri.2007.04.010).
- 520
- 521 Jeong, H.K., Gore, J.C., Anderson, A.W., 2013. High-resolution human
522 diffusion tensor imaging using 2-D navigated multishot SENSE EPI at 7
523 T. Magn. Reson. Med. 69, 793–802. doi:[10.1002/mrm.24320](https://doi.org/10.1002/mrm.24320).
- 524 Jones, D.K., 2010. Diffusion MRI: Theory, methods, and applications. Oxford
525 University Press. doi:[10.1093/med/9780195369779.001.0001](https://doi.org/10.1093/med/9780195369779.001.0001).

- 526 Katscher, U., Börnert, P., Leussler, C., van den Brink, J.S., 2003. Transmit
527 SENSE. Magn. Reson. Med. 49, 144–150. doi:[10.1002/mrm.10353](https://doi.org/10.1002/mrm.10353).
- 528 Knoll, F., Raya, J.G., Halloran, R.O., Baete, S., Sigmund, E., Bammer, R.,
529 Block, T., Otazo, R., Sodickson, D.K., 2015. A model-based reconstruction
530 for undersampled radial spin-echo DTI with variational penalties on the
531 diffusion tensor. NMR Biomed 28, 353–366. doi:[10.1002/nbm.3258](https://doi.org/10.1002/nbm.3258).
- 532 Lam, F., Li, Y., Peng, X., 2019. Constrained magnetic resonance spectro-
533 scopic imaging by learning nonlinear low-dimensional models. IEEE Trans.
534 Med. Imaging 39, 545–555. doi:[10.1109/TMI.2019.2930586](https://doi.org/10.1109/TMI.2019.2930586).
- 535 Le Bihan, D., Breton, E., Lallemand, D., Grenier, P., Cabanis, E., Laval-
536 Jeantet, M., 1986. MR imaging of intravoxel incoherent motions: appli-
537 cation to diffusion and perfusion in neurologic disorders. Radiology 161,
538 401–407. doi:[10.1148/radiology.161.2.3763909](https://doi.org/10.1148/radiology.161.2.3763909).
- 539 Liang, Z.P., 2007. Spatiotemporal imaging with partially separable functions,
540 in: 2007 4th IEEE International Symposium on Biomedical Imaging: From
541 Nano to Macro, pp. 988–991. doi:[10.1109/ISBI.2007.357020](https://doi.org/10.1109/ISBI.2007.357020).
- 542 Liu, C., Moseley, M.E., Bammer, R., 2005. Simultaneous phase cor-
543 rection and SENSE reconstruction for navigated multi-shot DWI with
544 non-Cartesian k -space sampling. Magn. Reson. Med. 54, 1412–1422.
545 doi:[10.1002/mrm.20706](https://doi.org/10.1002/mrm.20706).
- 546 Lustig, M., Donoho, D., Pauly, J.M., 2007. Sparse MRI: The application of
547 compressed sensing for rapid MR imaging. Magn. Reson. Med. 58, 1182–
548 1195. doi:[10.1002/mrm.21391](https://doi.org/10.1002/mrm.21391).

- 549 Mani, M., Jacob, M., Kelley, D., Magnotta, V., 2017. Multi-shot sensitivity-
550 encoded diffusion data recovery using structured low-rank matrix comple-
551 tion (MUSSELS). *Magn. Reson. Med.* 78, 494–507. doi:[10.1002/mrm.26382](https://doi.org/10.1002/mrm.26382).
- 553 Mani, M., Magnotta, V.A., Jacob, M., 2021. qModeL: A plug-and-play
554 model-based reconstruction for highly accelerated multi-shot diffusion MRI
555 using learned priors. *Magn. Reson. Med.* 86, 835–851. doi:[10.1002/mrm.28756](https://doi.org/10.1002/mrm.28756).
- 557 Mansfield, P., 1977. Multi-planar image formation using NMR spin echoes.
558 *J Phys C* 10, 55–58. doi:[10.1088/0022-3719/10/3/004](https://doi.org/10.1088/0022-3719/10/3/004).
- 559 Maudsley, A.A., 1980. Multiple-line-scanning spin density imaging. *J. Magn.*
560 *Reson.* 41, 112–126. doi:[10.1016/0022-2364\(80\)90207-3](https://doi.org/10.1016/0022-2364(80)90207-3).
- 561 Merboldt, K.D., Hanicke, W., Frahm, J., 1985. Self-diffusion NMR imag-
562 ing using stimulated echoes. *J. Magn. Reson.* 64, 479–486. doi:[10.1016/0022-2364\(85\)90111-8](https://doi.org/10.1016/0022-2364(85)90111-8).
- 564 Mori, S., Crain, B.J., Chacko, V.P., Van Zijl, P.C.M., 1999. Three-
565 dimensional tracking of axonal projections in the brain by mag-
566 netic resonance imaging. *Ann. Neurol.* 45, 265–269. doi:[10.1002/1531-8249\(199902\)45:2<265::AID-ANA21>3.0.CO;2-3](https://doi.org/10.1002/1531-8249(199902)45:2<265::AID-ANA21>3.0.CO;2-3).
- 568 Ong, F., Lustig, M., 2019. SigPy: A Python package for high performance
569 iterative reconstruction, in: Proceedings of the 27th Annual Meeting of
570 ISMRM, Montréal, CAN, p. 4819. doi:[10.5281/zenodo.5893788](https://doi.org/10.5281/zenodo.5893788).

- 571 Ong, F., Zhu, X., Cheng, J.Y., Johnson, K.M., Larson, P.E.Z., Vasanawala,
572 S.S., Lustig, M., 2020. Extreme MRI: Large-scale volumetric dynamic
573 imaging from continuous non-gated acquisitions. Magn. Reson. Med. 84,
574 1763–1780. doi:[10.1002/mrm.28235](https://doi.org/10.1002/mrm.28235).
- 575 Pipe, J.G., Farthing, V.G., Forbes, K.P., 2002. Multishot diffusion-weighted
576 FSE using PROPELLER MRI. Magn. Reson. Med. 47, 42–52. doi:[10.1002/mrm.10014](https://doi.org/10.1002/mrm.10014).
- 578 Polak, D., Splitthoff, D.N., Clifford, B., Lo, W.C., Huang, S.Y., Conklin, J.,
579 Wald, L.L., Setsompop, K., Cauley, S., 2022. Scout accelerated motion
580 estimation and reduction (SAMER). Magn. Reson. Med. 87, 163–178.
581 doi:[10.1002/mrm.28971](https://doi.org/10.1002/mrm.28971).
- 582 Porter, D.A., Heidemann, R.M., 2009. High resolution diffusion-weighted
583 imaging using readout-segmented echo-planar imaging, parallel imaging
584 and a two-dimensional navigator-based reacquisition. Magn. Reson. Med.
585 62, 468–475. doi:[10.1002/mrm.22024](https://doi.org/10.1002/mrm.22024).
- 586 Pruessmann, K.P., Weiger, M., Scheidegger, M.B., Boesiger, P., 1999.
587 SENSE: Sensitivity encoding for fast MRI. Magn. Reson. Med. 42, 952–
588 962. doi:[10.1002/\(SICI\)1522-2594\(199911\)42:5<952::AID-MRM16>3.0.CO;2-S](https://doi.org/10.1002/(SICI)1522-2594(199911)42:5<952::AID-MRM16>3.0.CO;2-S).
- 590 Ra, J.B., Rim, C.Y., 1993. Fast imaging using subencoding data sets from
591 multiple detectors. Magn. Reson. Med. 30, 142–145. doi:[10.1002/mrm.1910300123](https://doi.org/10.1002/mrm.1910300123).

- 593 Roemer, P.B., Edelstein, W.A., Hayes, C.E., Souza, S.P., Mueller, O.M.,
594 1990. The NMR phased array. Magn. Reson. Med. 16, 192–225. doi:[10.1002/mrm.1910160203](#).
- 595
- 596 Setsompop, K., Fan, Q., Stockmann, J., Bilgic, B., Huang, S., Cauley, S.F.,
597 Nummenmaa, A., Wang, F., Rathi, Y., Witzel, T., Wald, L.L., 2018. High-
598 resolution *in vivo* diffusion imaging of the human brain with generalized
599 slice dithered enhanced resolution: Simultaneous multislice (gSlider-SMS).
600 Magn. Reson. Med. 79, 141–151. doi:[10.1002/mrm.26653](#).
- 601 Setsompop, K., Gagoski, B.A., Polimeni, J.R., Witzel, T., Wedeen, V.J.,
602 Wald, L.L., 2012. Blipped-controlled aliasing in parallel imaging for si-
603 multaneous multislice echo planar imaging with reduced *g*-factor penalty.
604 Magn. Reson. Med. 67, 1210–1224. doi:[10.1002/mrm.23097](#).
- 605 Shafieizargar, B., Jeurissen, B., Poot, D.H.J., Klein, S., Van Audekerke,
606 J., Verhoye, M., den Dekker, A.J., Sijbers, J., 2023. ADEPT: Accurate
607 diffusion echo-planar imaging with multi-contrast shoTs. Magn. Reson.
608 Med. 89, 396–410. doi:[10.1002/mrm.29398](#).
- 609 Tournier, J.D., Smith, R., Raffelt, D., Tabbara, R., Dhollander, T., Pietsch,
610 M., Christiaens, D., Jeurissen, B., Yeh, C.H., Connelly, A., 2019. MRtrix3:
611 A fast, flexible and open software framework for medical image processing
612 and visualisation. NeuroImage 202, 116137. doi:<https://doi.org/10.1016/j.neuroimage.2019.116137>.
- 613
- 614 Trzasko, J., Manduca, A., 2011. Local versus global low-rank promotion in

- 615 dynamic MRI series reconstruction, in: Proceedings of the 19th Annual
616 Meeting of ISMRM, Montréal, CAN, p. 4371.
- 617 Tuch, D.S., Reese, T.G., Wiegell, M.R., Makris, N., Belliveau, J.W., Wedeen,
618 V.J., 2002. High angular resolution diffusion imaging reveals intravoxel
619 white matter fiber heterogeneity. Magn. Reson. Med. 48, 577–582. doi:[10.1002/mrm.10268](https://doi.org/10.1002/mrm.10268).
- 620
- 621 Uecker, M., Lai, P., Murphy, M.J., Virtue, P., Elad, M., Pauly, J.M.,
622 Vasanawala, S.S., Lustig, M., 2014. ESPIRiT – an eigenvalue approach
623 to autocalibrating parallel MRI: Where SENSE meets GRAPPA. Magn.
624 Reson. Med. 71, 990–1001. doi:[10.1002/mrm.24751](https://doi.org/10.1002/mrm.24751).
- 625 Wu, W., Koopmans, P.J., Andersson, J.L., Miller, K.L., 2019. Diffusion
626 Acceleration with Gaussian process Estimated Reconstruction (DAGER).
627 Magn. Reson. Med. 82, 107–125. doi:[10.1002/mrm.27699](https://doi.org/10.1002/mrm.27699).
- 628 Wu, W., Miller, K.L., 2017. Image formation in diffusion MRI: A review
629 of recent technical developments. J. Magn. Reson. Imaging 46, 646–662.
630 doi:[10.1002/jmri.25664](https://doi.org/10.1002/jmri.25664).
- 631 Zhang, T., Pauly, J.M., Levesque, I.R., 2015. Accelerated parameter mapping
632 with a locally low rank constraint. Magn. Reson. Med. 73, 655–661. doi:[10.1002/mrm.25161](https://doi.org/10.1002/mrm.25161).
- 633